

# A mathematical model of the erosion process in a channel bend

J. G. Herterich<sup>a,b</sup>, I. M. Griffiths<sup>c</sup>

<sup>a</sup>*School of Mathematics and Statistics, University College Dublin, Belfield, Dublin 4, Ireland*

<sup>b</sup>*Earth Institute, University College Dublin, Belfield, Dublin 4, Ireland*

<sup>c</sup>*Mathematical Institute, University of Oxford, Radcliffe Observatory Quarter, Oxford OX2 6GG, UK*

---

## Abstract

We develop a mathematical model for the cumulative erosion of a micro-particle in a channel system. At 90° bends in the system, a particle may deviate from the flow, impact the wall, and erode material. We highlight the case of the eroded material adhering to the particle, growing in size, and thus demonstrate how the damage accumulates exponentially with time. We describe and quantify the statistical nature of the evolution of particle growth and erosion (mass and location). We perform this analysis according to a number of realistic particle concentration distributions: uniform, Gaussian, and bimodal. A bimodal distribution, corresponding to the tubular pinch effect in suspension flows, results in unequal peak zones of erosion due to the flow characteristics.

*Keywords:* erosion; fluid–particle systems; discrete-to-continuum models

---

## 1. Introduction

Wear is a natural process for materials, arising as a result of interactions between surfaces. In piping systems, wear is often a result of corrosion, releasing solid particles, and erosion, by impact events<sup>?</sup>. Furthermore, as a feedback mechanism, the new surface defects can enhance the corrosion process<sup>?</sup> for a synergistic erosion–corrosion process<sup>?</sup>. Piping systems have a wide range of applications, encompassing household central-heating systems<sup>?</sup>, coolant systems for small photovoltaic systems<sup>?</sup>, and large tokamaks<sup>?</sup>. Pipe failure can be costly and catastrophic, from flooding of the home to termination of large-scale industrial projects. As a result, mathematical models that describe the key mechanisms for pipe wear are essential. The aim of this paper is to develop a mathematical model that describes the dominant contributions to pipe wear, to quantify the process and provide predictions that can act as safeguarding measures to avoid the aforementioned catastrophes.

Erosion is a physical process that induces the wear of materials, with many studies motivated by the oil and gas industry due to the erosive wear of equipment<sup>?</sup>. In piping systems, a ductile metal is impacted by a solid micro-particle in a fluid flow. Cutting and ploughing mechanisms form the basis of deformation and erosion modelling by impact<sup>?</sup>. In this paper, we use the cutting models of Finnie<sup>?</sup>. In pipe flow, erosion can occur by solid particles entrained in the flow striking the walls at bends due to their inertia and in straight sections due to turbulent mixing. There are many factors that may influence erosion, including: (i) particle size, shape, and concentration; (ii) surface properties of the pipe material, such as its yield

26 stress; and (iii) flow conditions, which determine the particle velocity and  
27 impact angle on the surface. It is observed that in systems where the flow  
28 conditions such as direction change rapidly, erosion is more prevalent than  
29 in straight pieces of pipes. This applies to pipe bends, turbine blades, and  
30 many other industrial processes<sup>?</sup>. An improved energy based erosion model  
31 incorporates surface material properties such as elastic modulus, Poisson's  
32 ratio, dynamic pressure, and coefficient of restitution<sup>?</sup>.

33 Particle dynamics in curved pipes has been studied for applications in  
34 aerosol science, regarding the deposition of particles<sup>?</sup><sup>?</sup>, as well as for ero-  
35 sion studies<sup>?</sup><sup>?</sup><sup>?</sup><sup>?</sup>. The erosion rate depends on the characteristics of:  
36 the individual particles; the suspension as a whole; the flow conditions; the  
37 erosion site; and the interaction during impact<sup>?</sup><sup>?</sup>. We note that although  
38 particles may erode from multiple sites when transported around a bend, the  
39 primary strike erodes more material than secondary strikes<sup>?</sup>. Furthermore,  
40 erosion rates decrease with pipe diameter at constant flow conditions<sup>?</sup>. In a  
41 gas–solid mixture, particle diameter and the radius of curvature of the bend  
42 influence the maximum erosion site<sup>?</sup>. Cheng and Wang<sup>?</sup> provide an ana-  
43 lytic solution for particle trajectories in an inviscid flow around a 90° bend,  
44 while turbulent flows may be described using  $k$ - $\epsilon$  turbulent flow models im-  
45 plemented in CFD packages<sup>?</sup> and gas–liquid flows often employ multiphase  
46 methods<sup>?</sup>. Chen *et al.*<sup>?</sup> compare erosion rates for elbow bends in liquid-  
47 particle flows, with 90° bend resulting in a larger incident angles but at  
48 lower velocities than 45° or 60° bends. Mansouri *et al.*<sup>?</sup> approximate a  
49 low-Reynolds-number flow near the wall to improve overprediction of erosion  
50 rates. Smoothed particle hydrodynamics may be used to simulate all damage

51 phenomena<sup>?</sup> .

52 Numerical studies to simulate the deposition and erosion–corrosion pro-  
53 cesses have been performed for idealized, potential, and parabolic flows in  
54 an elbow bend<sup>?</sup> , a U-bend<sup>?</sup> , a T-junction<sup>?</sup> and in other more com-  
55 plicated geometries<sup>?</sup> . Erosion–corrosion models usually combine separate  
56 models of the two processes<sup>?</sup> .

57 For a long and thin geometry, the flow is well described by a Poiseuille  
58 flow<sup>?</sup> . For a fully 3D viscous flow in a curved pipe, with radius of curvature  
59 of the bend large compared to the cross sectional radius of the pipe, the  
60 primary Poiseuille flow in the direction of the curved axis is complemented  
61 by a secondary flow of Dean vortices perpendicular to this axis due to the  
62 curvature<sup>?</sup> , as observed in experiments<sup>?</sup> . We neglect the effect of Dean  
63 vortices here and consider particle projections in 2D curved channels. A  
64 similar flow regime has been applied to viscous aerosol flow with moderate  
65 Reynolds numbers and a Stokes drag for the particles dynamics, with an  
66 Oseen correction applied for larger particles<sup>?</sup> .

67 Particles entrained in a flow collectively form a concentration distribution.  
68 Even in dilute systems, this concentration can have an effect on flow prop-  
69 erties such as viscosity<sup>?</sup> . However, for simplicity and to concentrate on the  
70 erosion aspect of this system, we neglect such considerations here. However,  
71 there are many other physical phenomena that occur in suspension dynam-  
72 ics<sup>?</sup> . The *tubular pinch effect* is an experimentally observed phenomenon  
73 whereby neutrally buoyant rigid spherical particles in a low-Reynolds-number  
74 Poiseuille flow through a straight circular tube tend to concentrate in an an-  
75 nular region around 0.6 tube radii from the axis in the tube<sup>?</sup> . The effect

76 has been simulated numerically for a two-dimensional channel flow, with two  
77 Gaussian particle distributions centred approximately halfway between the  
78 centre and the edge of the channel<sup>?</sup>. The effect has been illustrated for  
79 Reynolds numbers up to 2400, and occurs irrespective of the position at  
80 which the particle enters the tube<sup>?</sup>. However, the underlying mechanics  
81 that give rise to this phenomenon is still not fully understood<sup>???</sup>.

82 In this paper, we derive a mathematical model to explore the erosion  
83 process. We consider a specific geometry of a 90° two-dimensional channel  
84 bend and study the subsequent erosion. We model the flow of particles in a  
85 viscous fluid through a channel bend. We allow the particle to grow in mass as  
86 eroded material adheres to a particle that strikes a wall. We limit adhering to  
87 a small percentage of impacts since not all material will adhere in all cases<sup>?</sup>.  
88 Our simple model shows the effect of particle growth, encompassed with the  
89 Stokes number, on the erosion characteristics such as the site of maximum  
90 erosion.

91 We compare results with adhesion of eroded material to the impacting  
92 particle for 0, 2.5, 5, 7.5 and 10% of impacts to show the exponential growth  
93 in erosion for any amount of adhesion. Without adhesion, a particle causes  
94 the same amount of erosion on each impact, leading to a linear increase in  
95 eroded material. However, with a growing particle, we explain the exponen-  
96 tial growth in erosion in terms of increased inertia, causing a greater amount  
97 of erosion with subsequent impacts. Furthermore, an increase in mass alters  
98 the trajectory of a particle in the bend, leading to a non-trivial evolution in  
99 the location of the increased erosion. The model may be applied to real sys-  
100 tems, such as water flowing in copper piping systems, common in household

101 heating systems and industrial coolants. Specifically, the exponentially detri-  
102 mental erosion effects of a slowly growing particle would be seen in coolant  
103 systems designed to be untouched for decades, such as in tokamaks. Such  
104 results are prohibitively time consuming to obtain experimentally.

105 Regardless of whether they operate on small or large scales, the sys-  
106 tems discussed all comprise fluid flow in long-and-thin channels (aspect ratio  
107 1/100) under large pressures and flow rates, and hence large velocities (0.5–  
108 4 m/s)<sup>???</sup>. Table 1 contains some key parameters and their typical values  
109 with reference to a flow of water around a 90° bend with copper walls and a  
110 copper oxide corrosive product. Throughout the paper we use these values for  
111 reference in presenting results. We quantify erosion based on particle mass  
112 and position when entering the bend. We then use the results for a single  
113 particle to build a model for the erosion process. We conclude our analysis  
114 by discussing how the work presented in this paper can form a foundation  
115 for quantitatively predicting the erosion process in industrial settings.

## 116 **2. Model**

### 117 *2.1. Setup*

118 We consider the motion of particles in a section of a two-dimensional  
119 channel of width  $2\hat{a}$  making a 90° bend. Note we use the convention  $\hat{*}$  to  
120 denote dimensional quantities throughout this paper. In the 90° bend, let the  
121 centre of the channel have a radius of curvature  $\hat{R}$  and radii of curvature of  
122 the inner and outer walls are  $\hat{R} - \hat{a}$  and  $\hat{R} + \hat{a}$ , respectively (Figure 1). The  
123 flow enters and exits the bend from long straight sections, of typical length

Symbol	Description	Typical Value	Reference
$\hat{L}$	Length of straight section	1–10 m	
$\hat{R}$	Radius of curvature of a bend	5–25 cm	? ? ?
$2\hat{a}$	Width of a channel	0.1–5 cm	? ? ?
$\hat{a}_p$	Radius of a particle	100 $\mu\text{m}$	?
$\hat{U}_0$	Average flow velocity	0.5–4 $\text{m s}^{-1}$	? ? ? ?
$\hat{\rho}_{\text{Cu}}$	Density of copper Cu	8940 $\text{kg m}^{-3}$	
$\hat{\rho}_{\text{CuO}}$	Density of copper oxide CuO	6310 $\text{kg m}^{-3}$	
$\hat{\sigma}_{\text{Cu}}$	Flow stress of copper	10–200 MPa	?
$\hat{\mu}$	Dynamic viscosity of water	$1 \times 10^{-3}$ $\text{kg m}^{-1} \text{s}^{-1}$	
$\hat{\rho}$	Density of water	1000 $\text{kg m}^{-3}$	

Table 1: Table of notation, nomenclature, and typical values for the channel geometry, flow characteristics, and properties of copper, copper oxide, and water.

124  $\hat{L} \gg \hat{R} > \hat{a}$ . Some typical geometrical and physical values for the system are  
125 listed in Table 1. The feed flow into the bend has a large Reynolds number  
126  $\text{Re} = \hat{\rho}\hat{U}_0\hat{L}/\hat{\mu}$ , but for a long and narrow channel (with aspect ratio  $\delta =$   
127  $\hat{a}/\hat{L} \ll 1$ ), the reduced Reynolds number  $\delta^2\text{Re}$  is small. Hence a lubrication  
128 approximation is appropriate, whereby the transverse length-scale is small  
129 compared to the flow direction so that viscous and pressure forces dominate,  
130 thus simplifying the problem.

131 We set fluid and particles to enter the system at cylindrical polar coor-  
132 dinate angle  $\theta = 0$ , travelling anti-clockwise. We assume that the particles  
133 have had time to accelerate to the speed of the flow, at the particular entry  
134 point, before entering the bend. The subsequent bend in the channel, to-

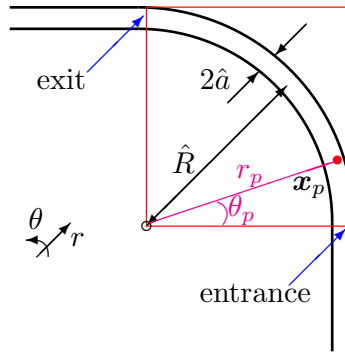


Figure 1: Schematic of channel geometry at a  $90^\circ$  bend (within box) with radius of curvature  $\hat{R}$  and width  $2\hat{a}$ . Long straight sections lead in and out of the bend. A particle traces a curve with location given in dimensionless variables (see §2.2 for details) by  $\mathbf{x}_p(t) = (r_p(t), \theta_p(t))$  in polar coordinates  $(r, \theta)$ . A closed loop consists of multiple corners joined together by the straight sections.



135 gether with the inertia of the particle, causes deviation and impact. Fluid  
 136 and particles exit the system at  $\theta = 90^\circ$ .

We assume the particles in our model to be spherical and small, of radius  $\hat{a}_p \ll \hat{a}$ , transported by the fluid tracing a position curve  $\hat{\mathbf{x}}_p(\hat{t}) = (\hat{r}_p(t), \theta_p(t))$  in cylindrical polar coordinates  $(\hat{r}, \theta)$ . The particles obey Stokes's law<sup>?</sup>, an expression for the frictional or drag force  $\hat{\mathbf{F}}$  exerted by a steady viscous fluid of velocity  $\hat{\mathbf{u}}(\hat{\mathbf{x}})$  on a small spherical particle of velocity  $d\hat{\mathbf{x}}_p/d\hat{t}$ ,

$$\hat{\mathbf{F}} = 6\pi\hat{\mu}\hat{a}_p \left( \hat{\mathbf{u}}(\hat{\mathbf{x}}_p) - \frac{d\hat{\mathbf{x}}_p}{d\hat{t}} \right), \quad (1)$$

137 where  $\hat{\mu}$  is the fluid viscosity. The force is linear in velocity and used  
 138 in modelling deposition of small particles in flows<sup>??</sup>. Non-laminar and  
 139 higher-Reynolds-number flows usually require a quadratic velocity-dependent  
 140 drag<sup>?</sup>, but we do not consider this here. A flow correction to Poiseuille flow  
 141 in a curved pipe, via a boundary layer, for a large Reynolds number and  
 142 small curvature is well established<sup>?</sup>.

143 We note that there will be an additional contribution to the force on the  
 144 particle due to the fact that it moves at a different velocity to the fluid as  
 145 it crosses the streamlines, pushing fluid away as it does so. For a particle  
 146 originating in the centre of the channel, the deviation from the streamlines  
 147 will be around half the width of the channel and will take place over a quarter  
 148 pipe length. This so-called added-mass force will therefore contribute an  
 149  $O(w/\pi R)$  correction to the result. Using the values given in Table 1 indicates  
 150 that this is typically only around 5%. We therefore neglect the effect here in  
 151 the interest of clarity of exposition of our study of the cumulative erosion,  
 152 but note that this could easily be incorporated into our analysis.

153 We model the transport and impact of individual particles. Particles

154 enter into the flow from the channel walls via corrosion due to oxidation or  
 155 erosion due to impact. However, corrosion occurs on a much longer timescale  
 156 compared with the typical time taken for a particle to flow through the  
 157 system<sup>?</sup>. The released material from impact can either appear as a separate  
 158 particle entrained in the flow or adhere to the striking particle<sup>??</sup>. While  
 159 the former adds particles that are negligibly small compared to the impacting  
 160 particle, the latter case is of interest as a cumulative erosion process grows  
 161 exponentially.

162 We combine an analysis for individual particles to simulate prescribed  
 163 concentration distributions. We demonstrate the process with three dis-  
 164 tributions: a uniform particle distribution, a Gaussian distribution, and a  
 165 bimodal distribution to represent the tubular pinch effect in a channel<sup>?</sup>.

## 166 2.2. Nondimensionalisation

In our model, we nondimensionalise the coordinates  $\hat{\mathbf{x}}$  and  $\hat{r}$ , particle  
 centre position  $\hat{\mathbf{x}}_p$  and  $\hat{r}_p$ , velocity  $\hat{\mathbf{u}}$ , and time  $\hat{t}$  variables with

$$\mathbf{x} = \frac{\hat{\mathbf{x}}}{\hat{a}}, \quad r = \frac{\hat{r}}{\hat{a}}, \quad \mathbf{x}_p = \frac{\hat{\mathbf{x}}_p}{\hat{a}}, \quad r_p = \frac{\hat{r}_p}{\hat{a}}, \quad \mathbf{u} = \frac{\hat{\mathbf{u}}}{\hat{U}_0}, \quad t = \frac{\hat{U}_0 \hat{t}}{\hat{a}}, \quad (2)$$

167 where  $\hat{U}_0$  is the mean flow speed. The dimensionless radius of curvature  
 168  $R = \hat{R}/\hat{a} = 8$  is such that the inner and outer walls are located at  $R - 1$   
 169 and  $R + 1$ , respectively. The domain is specified in cylindrical polar coordi-  
 170 nates by the dimensionless radial coordinate  $r \in [R - 1, R + 1]$  and angular  
 171 coordinate  $\theta \in [0, \pi/2]$ .

We consider particles in the system with initial mass  $\hat{m}_0$  and volume  $\hat{V}_0$ .  
 Particles grow in size, and we nondimensionalise their mass  $\hat{m}$ , volume  $\hat{V}$ ,

and volume eroded  $\hat{V}_e$  with respect to these initial values:

$$m = \frac{\hat{m}}{\hat{m}_0}, \quad V = \frac{\hat{V}}{\hat{V}_0}, \quad V_e = \frac{\hat{V}_e}{\hat{V}_0}, \quad (3)$$

172 where  $\hat{V} = 4\pi\hat{a}_p^3/3$  and the mass  $\hat{m} = \hat{\rho}_p\hat{V}$  with  $\hat{\rho}_p$  the particle density.

### 173 2.3. Particle motion

The motion of a spherical particle,  $\hat{\mathbf{x}}_p(\hat{t})$ , in a steady fluid flow,  $\hat{\mathbf{u}}(\hat{\mathbf{x}})$ , is described by Newton's second law,

$$\hat{m} \frac{d^2 \hat{\mathbf{x}}_p}{d\hat{t}^2} = \hat{\mathbf{F}}, \quad (4)$$

where  $\hat{\mathbf{F}}$  is the Stokesian drag force defined in (Eq. 1). Upon applying the nondimensionalisation (Eq. 2), the governing equation (Eq. 4) of motion becomes

$$\frac{d^2 \mathbf{x}_p}{dt^2} = \frac{1}{St} \left( \mathbf{u}(\mathbf{x}_p) - \frac{d\mathbf{x}_p}{dt} \right), \quad (5)$$

where  $St$  is the Stokes number, a dimensionless number measuring the characteristic time of the particle to that of the flow<sup>?</sup>, given by

$$St = \frac{2\hat{\rho}_p\hat{a}_p^2\hat{U}_0}{9\hat{\mu}\hat{a}} = \frac{\hat{U}_0}{6\pi\hat{\mu}\hat{a}} \left( \frac{4\pi\hat{\rho}_p}{3} \right)^{\frac{1}{3}} \hat{m}^{\frac{2}{3}}. \quad (6)$$

174 This relation gives a direct correspondence between the particle's inertia and  
 175 mass. For example, a Stokes number of 2 corresponds to a typical corroded  
 176 molecule from a copper pipe, such as copper oxide, CuO, with density  $\hat{\rho}_{\text{CuO}} =$   
 177  $6310 \text{ kg m}^{-3}$ , of radius approximately  $100 \mu\text{m}$  in a flow velocity of  $1 \text{ m/s}$   
 178 through a channel approximately  $1 \text{ cm}$  wide (Table 1).

The impact position and angle not only depend on the flow  $\mathbf{u}$  and Stokes number  $St$ , but also on the initial position  $\mathbf{x}_p(0)$  and velocity  $d\mathbf{x}_p(0)/dt$  when entering the bend. The particle's entry position is given by

$$\mathbf{x}_p(0) = \mathbf{x}_0. \quad (7)$$

In a long straight section of channel, it is reasonable to assume that a particle is accelerated to the flow speed itself, so

$$\frac{d\mathbf{x}_p(0)}{dt} = \mathbf{u}(\mathbf{x}_0). \quad (8)$$

The governing equations (Eq. 5), (Eq. 8) and (Eq. 7) for particle motion may be expressed in polar coordinates  $\mathbf{x}_p(t) = (r_p(t), \theta_p(t))$ . This leads to a coupled nonlinear second-order system of ordinary differential equations (ODEs) and initial conditions for  $r_p(t)$  and  $\theta_p(t)$ :

$$\frac{d^2 r_p}{dt^2} - r \left( \frac{d\theta_p}{dt} \right)^2 = -\frac{1}{St} \frac{dr_p}{dt}, \quad (9a)$$

$$r_p \frac{d^2 \theta_p}{dt^2} + 2 \frac{dr_p}{dt} \frac{d\theta_p}{dt} = \frac{1}{St} \left( u_\theta(r_p) - r_p \frac{d\theta_p}{dt} \right), \quad (9b)$$

$$\left. \begin{array}{l} r_p = R_0, \\ \theta_p = 0, \\ \frac{dr_p}{dt} = 0, \\ \frac{d\theta_p}{dt} = \frac{u_\theta(R_0)}{R_0}, \end{array} \right\} \text{at } t = 0 \quad (9c)$$

where  $\mathbf{x}_0 = (R_0, 0)$  for a radial entry position  $R_0$  at  $\theta_p = 0$  (Figure 1), and the dimensionless angular Poiseuille flow of unit flux is given by

$$u_\theta(r) = \frac{3}{2} \left( r(2R - r) - (R - 1)(R + 1) \right). \quad (10)$$

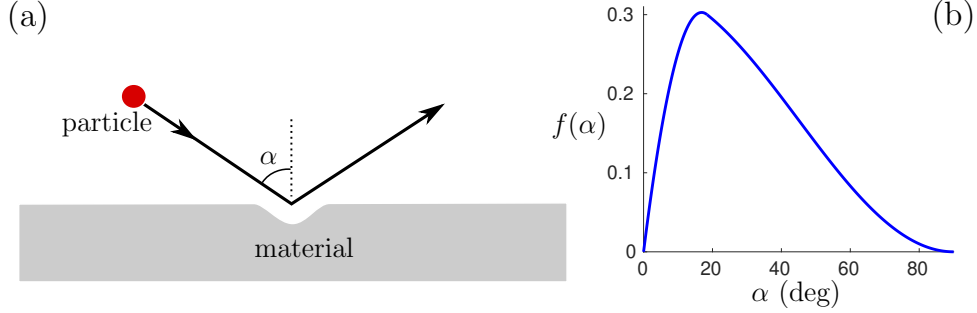


Figure 2: (a) Schematic of erosion as a cutting mechanism. (b) Impact angle-dependent function  $f(\alpha)$ , given by Eq. (12), for the volume eroded during impact (Eq. 14).

179 2.4. *Finnie's erosion model*

We model the erosion of ductile materials as an attacking cutting mechanism (Figure 2(a)). The amount of material eroded depends on how deep the particle can cut into the surface. The greater the kinetic energy of the particle, the deeper it cuts into the surface. Although kinetic energy (proportional to the square of the velocity) is the dominant contribution, particle rotation as it cuts into the surface contributes to an additional volume of material removed (a function of velocity cubed). The combination of the two may, however, be approximated by a single velocity exponent greater than two<sup>?</sup>. The angle of impingement,  $\alpha$ , influences the depth a particle can cut into the surface. The stronger the material, with flow stress  $\hat{\sigma}$ , under bombardment, the less it cuts into the surface. Finnie<sup>??</sup> combines these expectations to propose the following model for the volume  $\hat{V}_e$  of material eroded when a particle of mass  $\hat{m}$  strikes a metal surface with impact speed  $\hat{U}_i$ :

$$\hat{V}_e = \frac{\lambda \hat{m} \hat{U}_i^n f(\alpha)}{4\hat{\sigma}}. \quad (11)$$

180 Here,  $\lambda$  is an experimentally determined parameter, incorporating impact  
 181 characteristics such as fraction of particles cutting in the idealised man-  
 182 ner<sup>???</sup>. In the least material-dependent case<sup>?</sup>,  $\lambda$  has been determined  
 183 to be approximately equal to  $0.5 \text{ m}^{2-n} \text{ s}^{n-2}$ . The flow stress  $\hat{\sigma}$  for copper  
 184 is  $\hat{\sigma}_{\text{Cu}} = 10\text{--}200 \text{ MPa}$ <sup>?</sup>. The index  $n$  is typically in the range 2.3–2.4<sup>?</sup>.  
 185 However, a larger  $n$  is appropriate for a range of materials and suspension  
 186 properties<sup>??</sup>, as is found with a data fit to a dimensional analysis of volume  
 187 eroded<sup>?</sup>. Here we take  $n = 2.4$  and  $\lambda = 0.5 \text{ m}^{-0.4} \text{ s}^{0.4}$ .

The function  $f$  is an experimentally derived function

$$f(\alpha) = \begin{cases} \sin 2\alpha - 3 \sin^2 \alpha & \alpha < \alpha_0, \\ \frac{1}{3} \cos^2 \alpha & \alpha > \alpha_0, \end{cases} \quad (12)$$

188 accounting for the effect of the angle,  $\alpha$ , at which the striking particle impacts  
 189 relative to the perpendicular direction of the surface (Figure 2(b)). This cut-  
 190 ting mechanism causes maximum erosion for  $\alpha = \alpha_0 \approx 18.44^\circ$ . Particles  
 191 colliding perpendicularly with the material ( $\alpha \approx 0^\circ$ ) and particles that graze  
 192 the surface of the material tangentially ( $\alpha \approx 90^\circ$ ) do not erode any material.  
 193 Other similar functional forms for  $f$  are used<sup>?</sup>. An additional component for  
 194 plastic or visco-plastic deformation allows for non-zero erosion at high impact  
 195 angles<sup>??</sup>. This modification would affect most significantly the prediction  
 196 for particles that either strike at a grazing angle or strike close to perpendic-  
 197 ular to the channel wall. However, the detrimental effect of grazing strikes  
 198 will be negligible while strikes that are close to perpendicular to the channel  
 199 are unlikely to occur in our set-up. (The latter of these cases is confirmed in  
 200 Figure 3d.) Therefore, while important to acknowledge, such modifications  
 201 will not have a significant effect on the predictions on the erosive behaviour

202 in our model and so we do not include this effect here.

The impact angle is calculated by simple geometry from the solutions of the particle motion (Eq. 9)

$$\alpha = \frac{\pi}{2} - \theta_i + \tan^{-1} \left[ \frac{\frac{d}{dt}(r_p \cos \theta_p)}{\frac{d}{dt}(r_p \sin \theta_p)} \right]_{t=t_i}, \quad (13)$$

203 where  $\theta_i = \theta_p(t_i)$  is the angle at impact, and the time derivatives compute  
204 the limits for the angle as the moving particle approaches the wall.

Using the nondimensionalisation outlined in §2.2, equation (11) becomes

$$V_e = S_1 m U_i^n f(\alpha), \quad (14)$$

where recall that for a corroded copper oxide particle  $\hat{m} = \hat{\rho}_{\text{CuO}} \hat{V}_0$  and where  $S_1 = \lambda \hat{\rho}_{\text{CuO}} \hat{U}_0^n / 4 \hat{\sigma}_{\text{Cu}}$  and the dimensionless particle impact velocity in polar coordinates is given by

$$U_i = \left. \frac{d\mathbf{x}_p}{dt} \right|_{t=t_i} = \sqrt{\left( \frac{dr_p}{dt} \right)^2 + \left( r_p \frac{d\theta_p}{dt} \right)^2} \Bigg|_{t=t_i} \quad (15)$$

205 evaluated at impact time  $t_i$  based on particle motion (Eq. 9).

### 206 **3. Erosion in a channel bend**

207 We solve for the trajectory, impact, and erosion due to a single particle  
208 in a Poiseuille flow around a 90° bend in a channel. We note again that for  
209 a secondary strike within the bend the velocity and material eroded on the  
210 second strike is reduced<sup>?</sup>. This is also observed in our simulations, even with  
211 perfect restitution after the first impact. As such, we model only the first  
212 strike. We analyse the system by varying two parameters: the entry position  
213  $R_0$  and Stokes number  $St$ .

214 The governing system (Eq. 9) does not possess an analytic solution and  
 215 so we use a Runge–Kutta method to integrate the coupled ODEs. We com-  
 216 pare the impact characteristics for a range of parameters, particularly Stokes  
 217 numbers 2 and 5 for the full range of inlet positions  $R_1 < R_0 < R_2$ . The two  
 218 Stokes numbers provide a good comparison in terms of the difference in par-  
 219 ticle trajectories and impact characteristics, with  $St = 2$  already discussed as  
 220 typical for a  $100\ \mu\text{m}$  CuO particle, and  $St = 5$  for a particle with 60% more  
 221 mass. Particle deviation from the streamlines towards the outer channel wall  
 222 increases with Stokes number and decreases with entry point (Figure 3(a)).  
 223 The angular position  $\theta_i$  of impact for all entry points that impact the wall  
 224 is shown in Figure 3(b). It is not a linearly decreasing function due to the  
 225 quadratic nature of the Poiseuille flow, (Eq. 10). Particles entering the bend  
 226 on the inner half of the channel must traverse the faster flow region, and  
 227 hence gain speed. This is an important feature of this system. As the Stokes  
 228 number increases, the particle motion is less influenced by the flow, and im-  
 229 pact occurs at a lower angle (closer to the entrance to the bend), limited by  
 230  $\cos^{-1}(R_0/(R + 1))$ . Therefore, as particles grow in mass they subsequently  
 231 erode from a bend position tending towards that limit.

232 Impact velocity  $U_i$  (Eq. 15) and cutting angle  $\alpha$  (Eq. 13) are required to  
 233 quantify the volume eroded (Eq. 14). The impact velocity (Figure 3(c)) is  
 234 lower than its velocity at entry (Poiseuille flow, (Eq. 10), dashed), except for  
 235 particles entering close to the inner wall,  $R = R_1$ . Here, the entry velocity  
 236 is small but the particle speeds up as it traverses across the faster Poiseuille  
 237 flow. Particles with a larger Stokes number impact the wall with higher  
 238 velocities. The cutting angle  $\alpha$  decreases with Stokes number (Figure 3(d)).



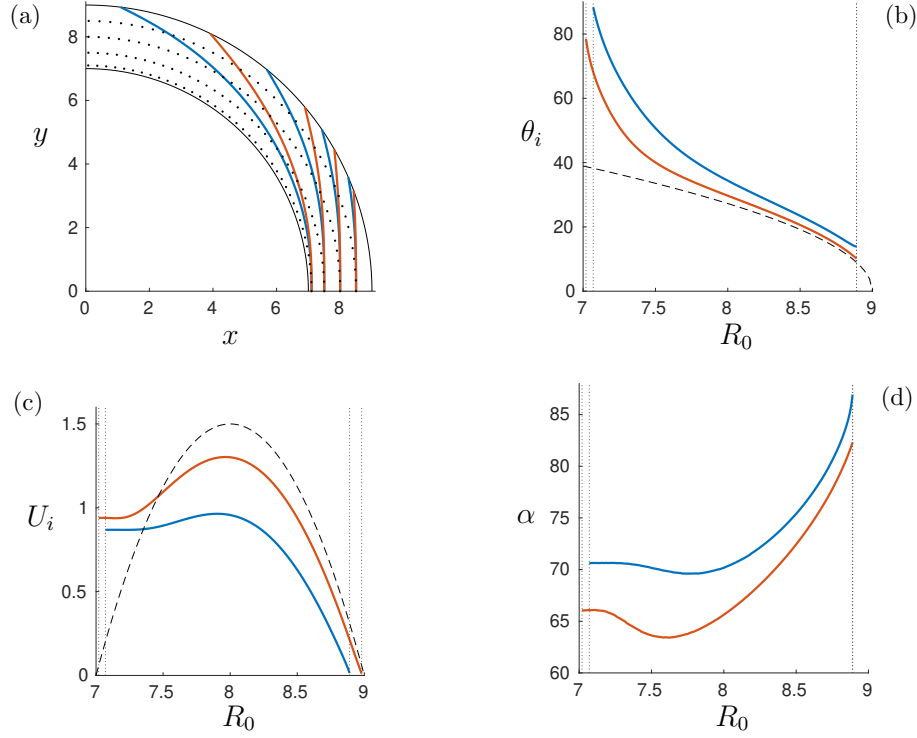


Figure 3: (a) Numerical solutions of CuO particle trajectories satisfying (Eq. 9) travelling anti-clockwise around a  $90^\circ$  bend in a channel, entrained in Poiseuille fluid flow. The particles enter at  $R_0 = 7.1, 7.5, 8.0, 8.5$  and strike the outer channel wall as they deviate from the streamlines (dotted). (b) Angular position  $\theta_i$  (degrees) of impact for entry position  $R_0$ , with limiting angle  $\cos^{-1}(R_0/(R+1))$  (dashed) for particles with  $St \gg 1$ . (c) Impact velocity  $U_i$  (Eq. 15) for particles entering at  $R_0$ , with the velocity at entry given by (Eq. 10) (dashed). (d) Impact angle  $\alpha$  (Eq. 13) for entry position  $R_0$ . Each figure contains results for Stokes numbers  $St = 2$  (blue) and  $5$  (red). The dotted lines in (b)–(d) represent the limiting entry points where impact occurs (Figure 5).

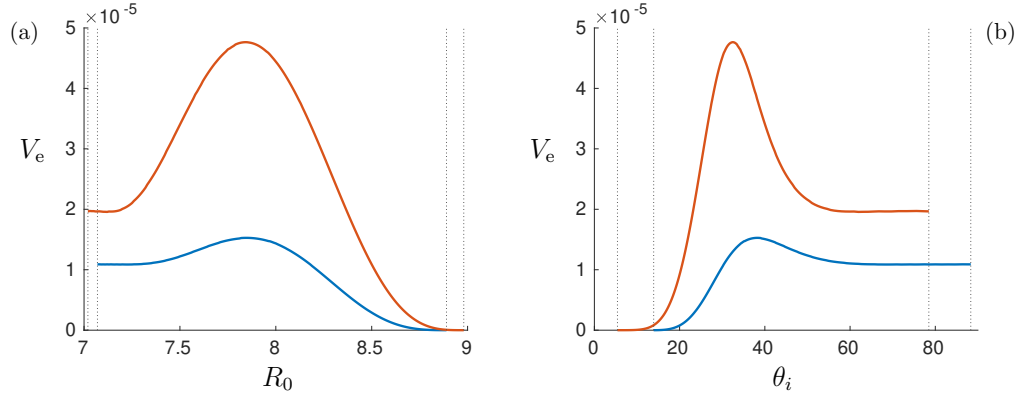


Figure 4: Volume of Cu eroded by CuO particles against (a) entry position  $R_0$  and (b) the impacting position  $\theta_i$  using (Eq. 9). Each figure contains results for Stokes numbers  $St = 2$  (blue) and 5 (red). The volume eroded is scaled by the initial volume of the impacting particle, which depends on the Stokes number, given by (Eq. 6). The dotted lines represent the limiting entry points where impact occurs (Figure 5).

239 We have observed that as the Stokes number  $St$ , or equivalently the mass  
 240  $m$  using (Eq. 6), increases, then so too does the velocity at impact  $U_i$ . Fur-  
 241 ther, since the cutting angle  $\alpha$  decreases, the function  $f(\alpha)$  (Eq. 12) also  
 242 increases. These all combine multiplicatively to increase the volume eroded  
 243  $V_e$ , (Eq. 14), as shown in Figure 4 for Cu walls eroded by impacting CuO par-  
 244 ticles. The volume eroded is maximised for particles entering left-of-centre  
 245 of the channel (Figure 4(a)), corresponding to the largest impact velocities  
 246 (Figure 3(c)) and smaller cutting angles (Figure 3(d)). Furthermore, this  
 247 region of greatest erosion occurs in the channel bend outer wall between  $30^\circ$   
 248 and  $50^\circ$ . As the Stokes number increases, the range of impact positions  $\theta_i$   
 249 decreases (Figure 4(b)).

250 The volume eroded scales with  $S_1 \approx 10^{-5}$  using (Eq. 14), and thus is small  
 251 compared with the total particle mass. If this eroded material were to enter  
 252 into the flow as its own particle, then this would have a Stokes number  $St \ll 1$   
 253 and would thus follow the streamlines. However, as discussed, we suppose  
 254 that in a fraction of cases the eroded material adheres to the impacting  
 255 particle<sup>?</sup> <sup>?</sup>, thus increasing the mass (and Stokes number) of that particle.  
 256 For simplicity we assume the particle remains spherical. After a full cycle  
 257 in the closed channel system, the now larger particle re-enters the bend.  
 258 However, if it enters at the same entry point, it does not collide with the  
 259 wall at the same position  $\theta_i$  (Figure 3(b)) because the Stokes number for the  
 260 motion governed by (Eq. 9) has increased. An increased amount of material is  
 261 subsequently eroded at the updated point (Figure 4) as the additional kinetic  
 262 energy of a larger particle makes up for any decrease in  $f(\alpha)$  (Eq. 14). This  
 263 process repeats itself, with long-term cumulative damage being exponential  
 264 and thus detrimental to the structural integrity of the channel. We model  
 265 this in the following section.

266 Note that not all particles impact the wall: there exists a region near the  
 267 outer wall for which particles that enter in this region never strike the wall of  
 268 the bend, with limiting entry point  $R_0^*$ . As a particle approaches the channel  
 269 wall, the fluid flow speed is decreasing, and the particle may lose sufficient  
 270 inertia before striking the wall such that that it follows the streamlines. The  
 271 size of this region depends on the Stokes number (Figure 5(a)). For  $St < 0.95$ ,  
 272 no particles impact the wall as they remain entrained within the flow. When  
 273  $St = 1$ , less than half the entry points results in particle impact with the  
 274 wall. For  $St > 2$  the effect is negligible as only an extremely narrow range of

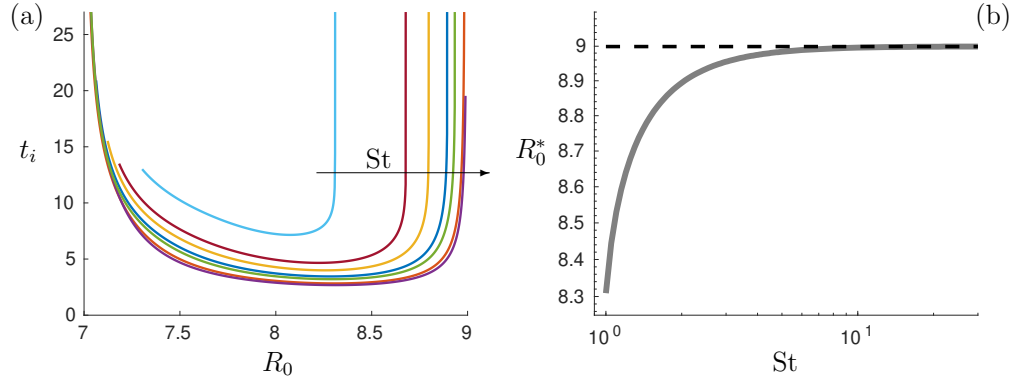


Figure 5: (a) Impact time  $t_i$  by entry point  $R_0$  for Stokes numbers  $St = 1, 1.25, 1.5, 2, 2.5, 5,$  and  $10$ . Particles entering the channel near either wall may not impact the outer wall ( $t_i \rightarrow \infty$ ). (b) Limiting right-sided entry point  $R_0^*$  for impact. Cases of  $R_0^* < R_2 = 9$  correspond to infinite gradients in the curves in (a).

275 particle entry points do not impact the wall. For  $St > 10$ , impact occurs at  
 276 all particle entry positions (Figure 5(b)). Analogously, particles entering the  
 277 bend near the inner wall ( $R_0 - 1$ ) may not gain sufficient inertia to traverse the  
 278 channel within the length of the bend, exiting the bend at  $\theta = 90^\circ$ . Particles  
 279 entering the bend with lower values of  $R_0$  must travel further (Figure 3(a)),  
 280 and may impact the wall at similar times to those that enter at larger values  
 281 of  $R_0$ . This is also a consequence of the Poiseuille flow profile.

#### 282 4. Particle Growth in a Closed Bend

283 In the previous section, we related the Stokes number  $St$  (Eq. 6), inlet  
 284 position  $R_0$ , impact position  $\theta_i$ , and volume eroded  $V_e$  (Eq. 14) during particle  
 285 impact in a  $90^\circ$  bend. Now we consider the repeated impact of such a particle

286 in a closed piping system. We analyse its rate of growth, where the eroded  
287 material adheres to the striking particles. We assume that the shape of  
288 the resulting particle is also spherical. This assumption is reasonable since,  
289 after many collisions of this type, we expect the shape to be spherical on  
290 average. The density of the particle, originally copper oxide with eroded  
291 copper adhering, must be updated with each strike. In this section, for  
292 illustrative purposes of the discrete and continuum models to be employed  
293 later, we assume that all the eroded material adheres to the particle.

294 We first model the system as a series of discrete impacts in §4.1 and then  
295 take the continuous limit in which the particle mass grows continuously in  
296 time in §4.2. The results help quantify the spatial-temporal damage caused to  
297 the channel wall. However, in §5 we consider a more realistic approach. The  
298 assumptions remain valid until such a time that the flow may be classified as  
299 a slurry whereby the particle suspension has an effect on the flow properties  
300 and particle interactions become significant<sup>?</sup>.

#### 301 *4.1. Discrete model*

We track the accumulation of mass for one particle with each striking of the channel wall. We suppose that on the  $i^{\text{th}}$  passage, the particle enters the bend from the same position  $R_0$  with mass  $m_i$  and volume  $V_i$  and has Stokes number  $St_i$ . After each strike the particle increases in mass, volume

and Stokes number which are accordingly updated

$$V_{j+1} = V_j + V_{e_j}, \quad (16a)$$

$$\text{St}_{j+1} = \left( \frac{V_{j+1}}{V_j} \right)^{\frac{2}{3}} \text{St}_j, \quad (16b)$$

$$m_{j+1} = m_j + \frac{\hat{\rho}_{\text{Cu}}}{\hat{\rho}_{\text{CuO}}} V_{e_j}, \quad (16c)$$

302 where  $V_{e_j}$  is the volume eroded at strike  $j$  (if it does impact the wall). The  
 303 volume eroded  $V_{e_i}$ , given by (Eq. 14), is dependent on the mass, and hence  
 304 increases with the Stokes number (Eq. 6).

#### 305 4.2. Continuous Model

306 The increase in volume observed after each strike compared with the  
 307 volume of the particle before impact is small,  $\mathcal{O}(S_1) = \mathcal{O}(10^{-5})$  (Figure 4).  
 308 We thus consider these increases as infinitesimal to allow us to model the  
 309 process continuously.

We substitute for  $V_{e_j}$  using (14) in (16c) to give

$$\frac{m_{j+1} - m_j}{S_1} = \frac{\rho_{\text{Cu}}}{\rho_{\text{CuO}}} m_j U_i^n f(\alpha). \quad (17)$$

Taking the limit  $S_1 \rightarrow 0$  allows us to identify the left-hand expression as a  
 continuous derivative  $dm/dt$  where the timescale  $t$  is connected to the discrete  
 model by the fact that  $t = S_1$  after one strike. We then obtain an ordinary  
 differential equation describing the growth over the erosion timescale:

$$\frac{dm}{dt} = \frac{\rho_{\text{Cu}}}{\rho_{\text{CuO}}} m U_i(m)^n f(m), \quad (18)$$

310 where we the impact velocity  $U_i$  and the function  $f$  are functions of  $m$  that  
 311 we determine numerically (see Figures 3(c) and 3(d) respectively).

312 *4.3. Comparison*

313 We compare the discrete (Eq. 16) and continuous (Eq. 18) models accord-  
314 ing to Algorithm 1 (below). We implement both models over 20,000 impacts,  
315 and observe good agreement before they diverge after a 20% increase in mass,  
316 regardless of inlet position (Figure 6). The number of strikes after which this  
317 occurs depends on the inlet position  $R_0$ .

---

**Algorithm 1** Calculating particle growth via the discrete (Eq. 16) and con-  
tinuous (Eq. 18) models.

---

**Input:** Particle with initial Stokes number  $St = 2$  and entry position  $R_0$

- 1: **for** each impact **do**
- 2: Solve particle dynamics system (Eq. 9)
- 3: Determine volume eroded  $V_e$  (Eq. 14) and erosion site  $\theta_e$
- 4: Determine mass  $m(t)$  of particle for discrete (Eq. 16)/continuous (Eq. 18)  
models
- 5: Update Stokes number (Eq. 6)
- 6: **end**

**Output:**  $m(t)$

---

318 Moreover, we observe a dramatic difference in growth depending on entry  
319 position  $R_0$ . This is a result of the Poiseuille flow (Eq. 10). Particles entering  
320 with  $R_0 < R$  traverse the faster fluid and speed up before impact with the  
321 outer wall compared to those entering with  $R_0 > R$  (see Figure 3c). Those  
322 higher speeds results in greater erosion (Eq. 14). However, as particles loop  
323 around a closed system, they do not enter the same bend at that same entry  
324 point. This necessarily means a growth rate that must be averaged over entry

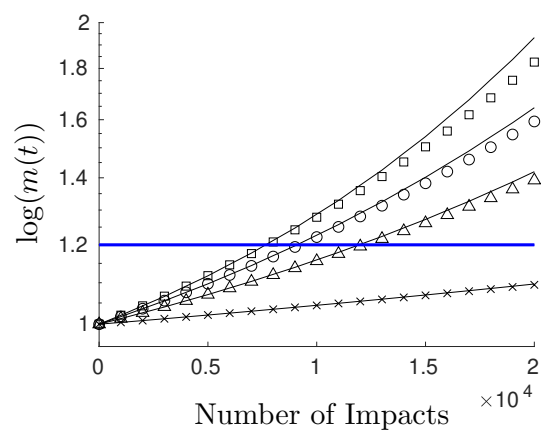


Figure 6: Particle growth  $m(t)$  on a log scale over 20,000 impacts, showing a greater than exponential rate. Growth via the discrete model (Eq. 16) with  $R_0 = 7.5$  ( $\circ$ ), 8 ( $\square$ ), 8.25 ( $\triangle$ ), and 8.5 ( $\times$ ) and corresponding continuous model (Eq. 18) (solid) begin to diverge after an approximate 20% (horizontal line) growth in mass.



325 positions. We address this in the next section.

## 326 **5. Statistics of a single particle**

### 327 *5.1. Inlet distributions*

In general, a particle suspension entering a channel bend will be well mixed according to a probability distribution of inlet positions,  $R_0$ , say  $g(R_0)$ , where  $g(R_0)$  satisfies the required probability constraint,

$$\int_{R-1}^{R+1} g(R_0) dR_0 = 1. \quad (19)$$

328 In this section, we simulate the recurring entry of a particle into a bend where  
329 now each return and re-entry of the particle is at a different location according  
330 to  $g$ . This more realistic situation lends itself to a statistical description of  
331 the erosion caused by an individual particle over a long time in the channel.

332 Again, the particle may impact the wall and erode mass. That mass  
333 may either adhere to the particle so that it grows in mass, for a fraction  
334  $\chi$  of impacts. Otherwise it enters the flow and, as a relatively small mass,  
335 follows the streamlines (Figure 4) and thus does not contribute further to  
336 the erosion. However, for each simulation of a particle entering the bend, we  
337 use a random number generator to determine the subsequent entry position  
338  $R_0$  on each cycle according to the inlet location distribution  $g(R_0)$ . We  
339 calculate the impact position and mass eroded at each cycle using the discrete  
340 model (Eq. 16) for greater accuracy. We use a uniform random number to  
341 determine if this impact is one of the fraction  $\chi$  that results in adhesion to  
342 the impacting particle, and hence a growing particle. We simulate 250,000  
343 cycles, representing the long-term evolution within a sealed coolant system,

344 and perform this analysis for many particles. If a particle does not strike  
345 the wall, no erosion occurs. We determine the statistical distribution of  
346 impact locations, volume eroded by a particle, and particle growth. The  
347 process is summarised in Algorithm 2 (below). As such, we determine an  
348 average of the dynamics of erosion caused by a single particle: mass eroded;  
349 location of erosion; and particle growth. With this statistical representation  
350 of erosion due to a single particle from a distribution, the erosion caused  
351 by many particles from a suspension can be determined by scaling up the  
352 results to many particles as they are released into the system. Furthermore,  
353 we compare the influence of different levels of eroded material adhering to  
354 the particle.

---

**Algorithm 2**

---

**Input:** Particle with Stokes number  $St = 2$

- 1: Bend entry position randomised from a distribution  $g$  (Eq. 20)
- 2: Solve particle dynamics system (Eq. 9)
- 3: Record the cumulative volume eroded  $V_e$  (Eq. 14) and erosion site  $\theta_e$  with  
1 degree bins
- 4: Use a uniform random number to determine if each impact is one of frac-  
tion  $\chi$  that results in eroded material adhering to the impacting particle
- 5: If particle growth occurs, update Stokes number (Eq. 6)
- 6: Repeat Steps 1 – 5 with entry position for growing particle randomised  
from the same distribution for 250,000 entries
- 7: Repeat Steps 1 – 6 for  $M$  different particles

**Output:** Statistics on location and volume of material eroded by a growing  
particle

---

We consider three distributions  $g$  – uniform, normal, and bimodal (*tubular pinch effect*) – for illustration of the differing effects on the erosion of the channel wall:

$$g = \begin{cases} \mathcal{U}(R_0) = \frac{1}{2}, & \text{Uniform} \\ \mathcal{N}(R_0, \nu) = \frac{e^{-(R_0-R)^2/2\nu^2}}{\int_{R-1}^{R+1} e^{-(R_0-R)^2/2\nu^2} dR}, & \text{Normal} \\ \mathcal{B}(R_0, q, \nu) = \frac{e^{-(R_0-R+q)^2/2\nu^2} + e^{-(R_0-R-q)^2/2\nu^2}}{\int_{R-1}^{R+1} e^{-(R_0-R+q)^2/2\nu^2} + e^{-(R_0-R-q)^2/2\nu^2} dR}, & \text{Bimodal.} \end{cases} \quad (20)$$

355 Here,  $\mathcal{U}(R_0)$  is the uniform distribution for all entry points,  $\mathcal{N}(R_0, \nu)$  is the  
 356 normal distribution centred in the middle of the channel with variance  $\nu$  and  
 357  $\mathcal{B}(R_0, q, \nu)$  is a bimodal distribution given by two Gaussian distributions,  
 358 both with variance  $\nu$ , centred at a distance  $q$  from the centre of the channel  
 359 to each wall, *i.e.*, at  $R \pm q$ . In all simulations we conduct we take  $q = 0.5$   
 360 and  $\nu = 0.4$  for the Gaussian distribution and  $\nu = 0.2$  for the bimodal  
 361 distribution. We illustrate these distributions in Figure 7.

362 The location and cumulative mass eroded is averaged over  $M$  initially  
 363 identical particles for 250,000 cycles to obtain the statistics representing the  
 364 erosion capabilities of a single particle. We consider the average statistics for  
 365  $M = 20$ , with a normed relative error of  $\mathcal{O}(10^{-3})$  in mass eroded between  
 366  $M = 20$  and  $M = 21$ . The probability density functions for the impact  
 367 location of a striking particle, for each inlet distribution function (Eq. 20)  
 368 as the particle grows in size. We first discuss total cumulative erosion over  
 369 the whole bend and particle growth, and later analyse the evolution of the  
 370 distribution of impact locations as an impacting particle grows. We consider

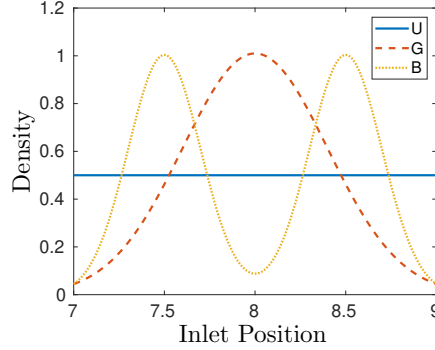


Figure 7: Particle inlet distributions given by uniform (U), Gaussian (G) with  $\nu = 0.4$ , and bimodal (B) with  $\nu = 0.2$  and  $q = 0.5$ , as given in (Eq. 20).

371 the cases of eroded material adhering to the impacting particle for  $\chi =$   
 372 0, 2.5, 5, 7.5, and 10% of cases.

### 373 5.2. Cumulative erosion and growth

374 We simulate Algorithm 2, obtaining the statistics for erosion by a sin-  
 375 gle particle. The cumulative mass eroded from the channel wall by one  
 376 particle grows to many times the initial particle mass over 250,000 impacts  
 377 (Figures 8a, 9a, 10a). The cumulative mass grows linearly with strikes for  
 378  $\chi = 0\%$ , but exponentially when  $\chi > 0\%$ . The ranges for mass eroded after  
 379 250,000 impacts for  $\chi \in [0, 10]\%$  are: [3.0, 4.9] for the uniform case, [3.8, 7.5]  
 380 for the Gaussian case, and [2.9, 4.6] for the bimodal case.

381 We see the exponential growth more clearly through the excess erosion  
 382 relative to  $\chi = 0\%$  in the system. Adhesion of eroded material to the im-  
 383 impacting particle is significant (Figures 8b, 9b, 10b). The ranges for excess  
 384 mass eroded after 250,000 impacts for  $\chi \in [2.5, 10]\%$  are: [0.35, 1.9] for the

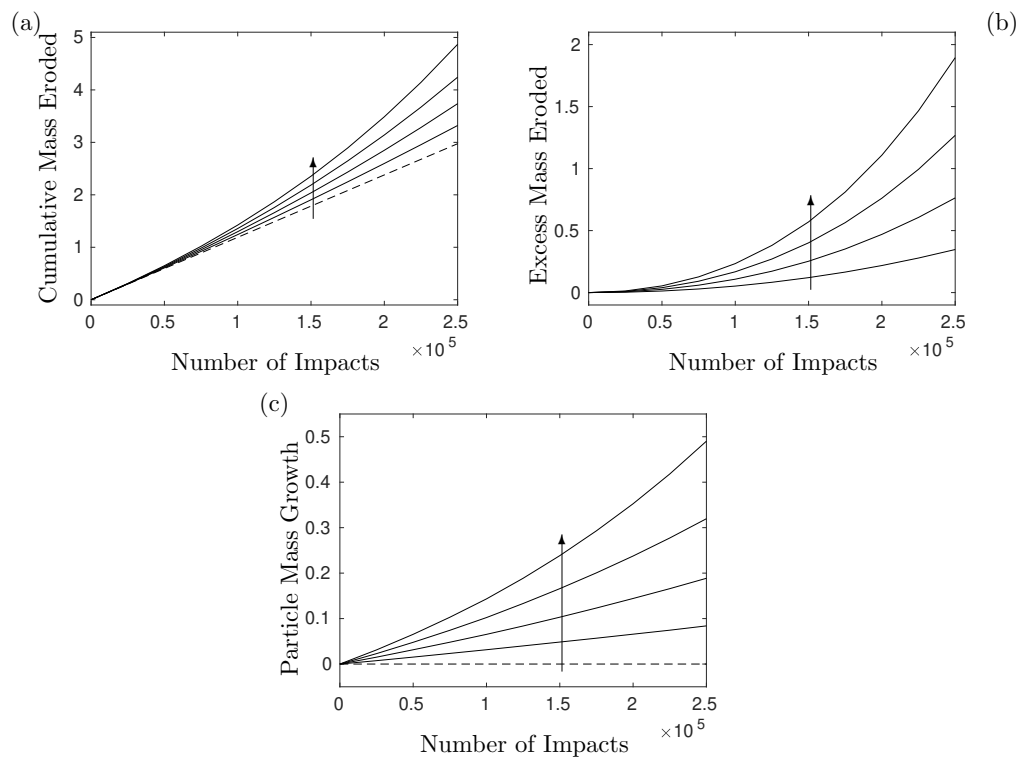


Figure 8: Evolution of erosion for the uniform inlet distribution (20a). (a) Cumulative mass eroded from the wall for  $\chi = 0, 2.5, 5, 7.5,$  and  $10\%$ , with  $\chi = 0\%$  the dashed line. (b) Excess mass, relative to  $\chi = 0\%$ , eroded by a growing particle for  $\chi = 2.5, 5, 7.5,$  and  $10\%$ . (c) Particle growth for  $\chi = 0, 2.5, 5, 7.5,$  and  $10\%$ , with  $\chi = 0\%$  the dashed line. The arrows point to increasing  $\chi$ .

385 uniform case,  $[0.58, 3.6]$  for the Gaussian case, and  $[0.32, 1.7]$  for the bimodal  
386 case. In fact, the exponential growth of  $A \exp \lambda t$  is such that the amplitude  
387  $A$  has a strong dependence on  $\chi$  and the growth rate  $\lambda$  has weak dependence  
388 on  $\chi$ .

389 The particle mass grows due to adhesion of eroded material (Figures 8c,  
390 9c, 10c). The ranges for particle mass growth after 250,000 impacts for  
391  $\chi \in [0, 10]\%$  are:  $[0.49]$  for the uniform case,  $[0, 0.74]$  for the Gaussian case,  
392 and  $[0, 0.46]$  for the bimodal case. Note that these numbers scale correctly  
393 with the excess erosion according to  $\chi$ .

394 Qualitatively similar results are observed for the three distributions. How-  
395 ever, while the erosion and particle growth rates are similar for the uniform  
396 and bimodal distributions, with uniform causing more damage than the bi-  
397 modal, the Gaussian distribution causes significantly more damage with a  
398 faster growth rate. This is a result of the single central peak distribution  
399 (Figure 7) leading to more particles entering the bend in the faster flowing  
400 region of the channel (Figure 3).

401 Growth in particle mass  $m$  is directly related to the Stokes number  $St$ ,  
402 with  $St \sim m^{2/3}$  (6). We observe the Stokes number increasing for all  $\chi > 0$  as  
403 expected (Figure 11). It is this relationship between mass and Stokes number  
404 that affects the evolution of dynamics (Figure 3) and erosion amount and  
405 location (Figure 4). We analyse this in the next section.

### 406 *5.3. Location of impact and erosion*

407 In the previous section, we considered the cumulative effect of erosion  
408 in the bend. Here we discuss the details within that, namely the impact

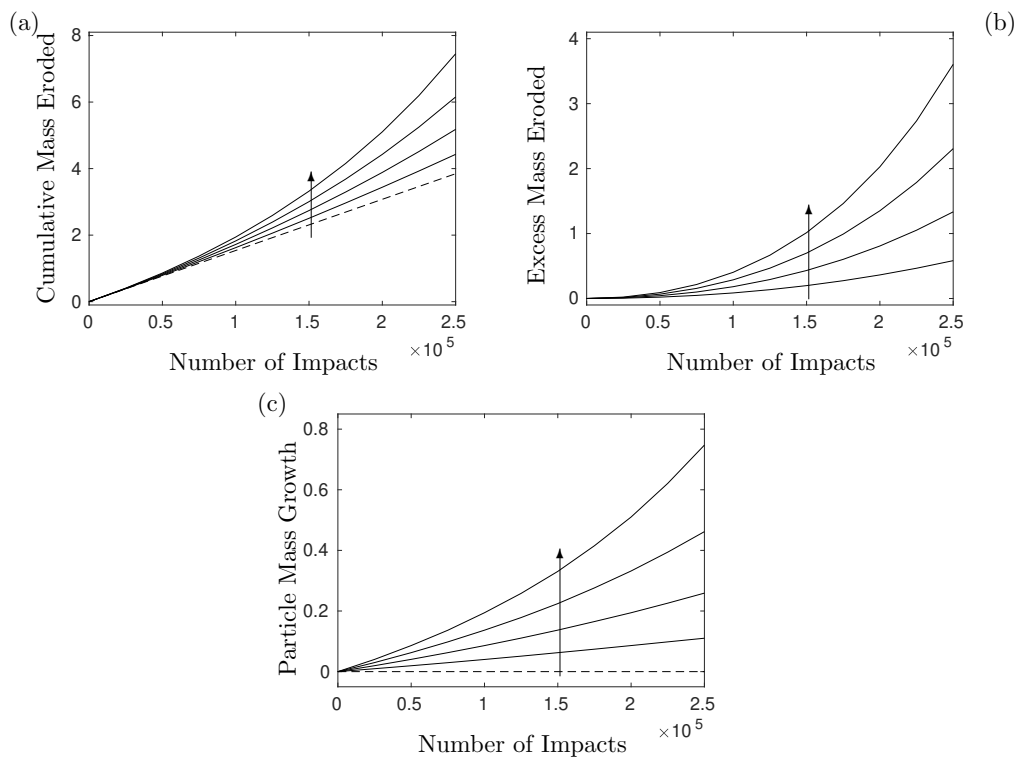


Figure 9: Evolution of erosion for the Gaussian inlet distribution (20b). (a) Cumulative mass eroded from the wall for  $\chi = 0, 2.5, 5, 7.5,$  and  $10\%$ , with  $\chi = 0\%$  the dashed line. (b) Excess mass, relative to  $\chi = 0\%$ , eroded by a growing particle for  $\chi = 2.5, 5, 7.5,$  and  $10\%$ . (c) Particle growth for  $\chi = 0, 2.5, 5, 7.5,$  and  $10\%$ , with  $\chi = 0\%$  the dashed line. The arrows point to increasing  $\chi$ .

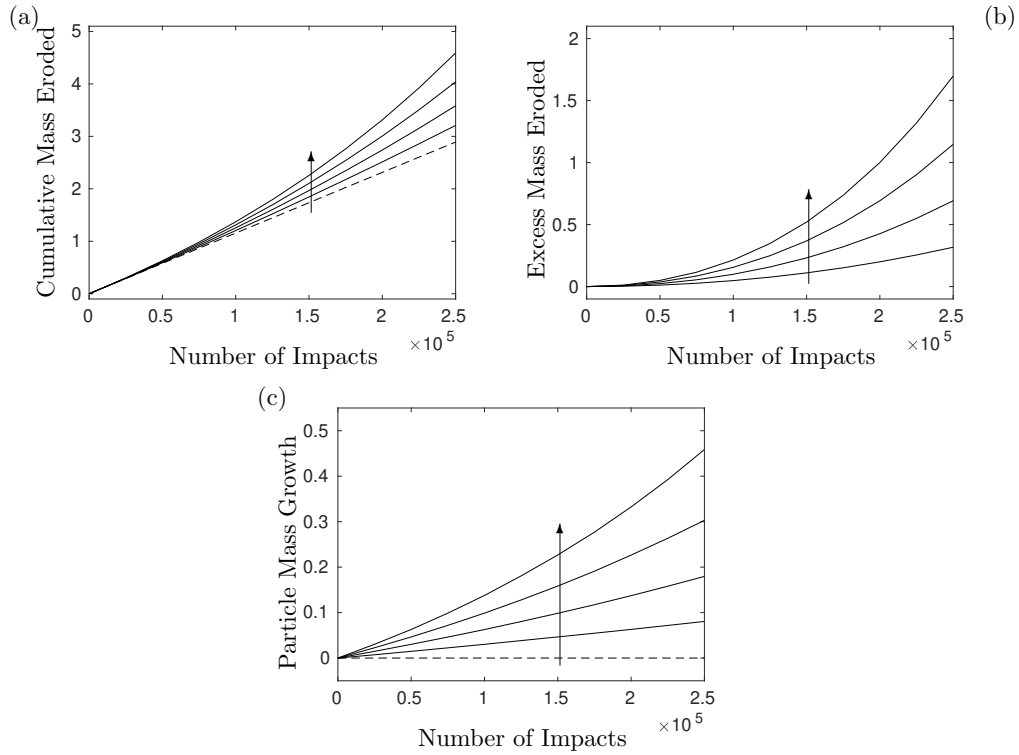


Figure 10: Evolution of erosion for the bimodal inlet distribution (20c). (a) Cumulative mass eroded from the wall for  $\chi = 0, 2.5, 5, 7.5$ , and  $10\%$ , with  $\chi = 0\%$  the dashed line. (b) Excess mass, relative to  $\chi = 0\%$ , eroded by a growing particle for  $\chi = 2.5, 5, 7.5$ , and  $10\%$ . (c) Particle growth for  $\chi = 0, 2.5, 5, 7.5$ , and  $10\%$ , with  $\chi = 0\%$  the dashed line. The arrows point to increasing  $\chi$ .



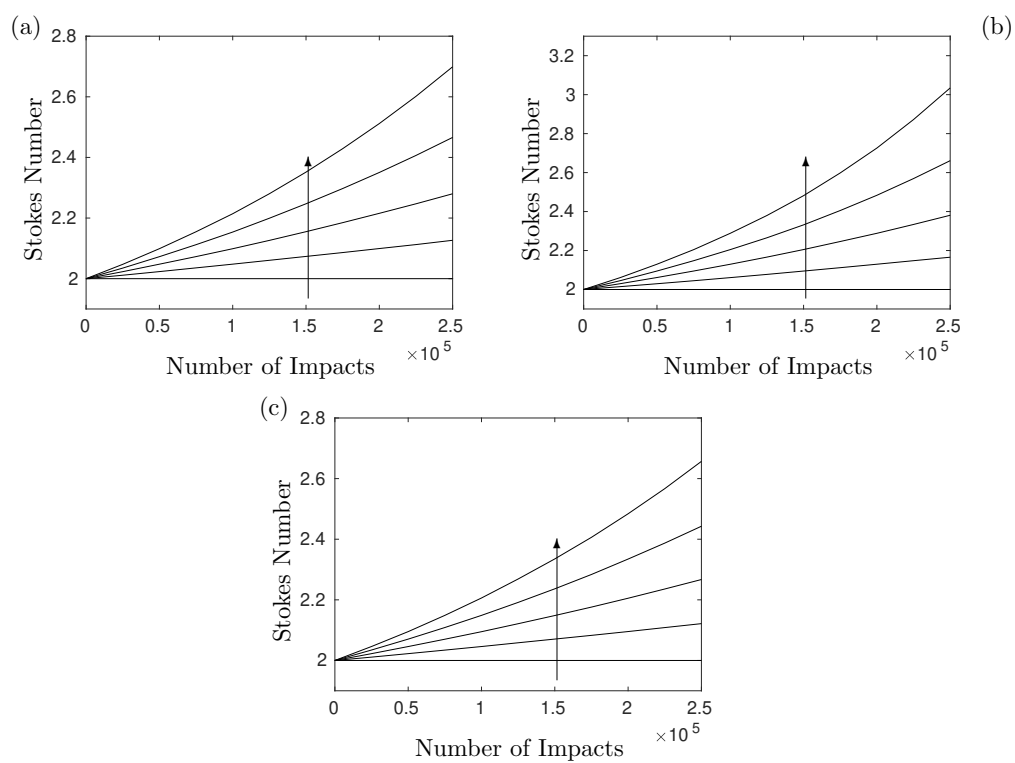


Figure 11: Growth of Stokes number for (a) uniform, (b) Gaussian, and (c) bimodal distributions (20). The arrows point to increasing  $\chi = 0, 2.5, 5, 7.5,$  and  $10\%$ .

409 frequency and mass eroded by location in the bend. We analyse the evolution  
410 of this process with a growing particle.

411 For brevity and illustrative purposes we consider results for  $\chi = 10\%$ .  
412 We show the probability density function (PDF) of impact locations as the  
413 number of impacts increases in Figures 12(a,b,c). For reference, with  $\chi = 0\%$   
414 there would be no change in the PDF. The corresponding statistical time-  
415 cumulative mass eroded by location in the bend is shown in Figures 12(d,e,f),  
416 respectively. We use a moving average to smooth the data: the average is  
417 computed with a window, a sliding vector of elements, of length 10 about  
418 each point representing  $1^\circ$ , and the average is computed with a Gaussian  
419 weighting. The results we discuss are qualitatively similar for lower values of  
420  $\chi$ , but the effects are less pronounced; more impacts are required to observe  
421 similar behaviour.

422 The statistics of the impact position for each inlet distribution (Fig-  
423 ures 12(a-c)) shift to lower values of  $\theta_i$  as the number of cycles increases, as  
424 expected with growing particles (Figure 3(b)), increasing in mass for  $\chi = 10\%$   
425 of impacts in this case. This increases the inertia of the particle, via the  
426 Stokes number as discussed in the previous section, so that the particles de-  
427 viate more from the streamlines as evidenced in Figure 3(a). The variation,  
428 however, is non-trivial and depends on the inlet distribution (Eq. 20).

429 Particles entering on the inner half of the channel, with  $R_0 < R$ , tra-  
430 verse through the faster-flowing fluid (Figure 3(c)) and are spread out to a  
431 larger degree further along the bend (Figure 3(a,b)) than those entering on  
432 the outer half of the channel, with  $R_0 > R$ . This affects the impact distri-  
433 bution, with a more concentrated impact region for particles entering with

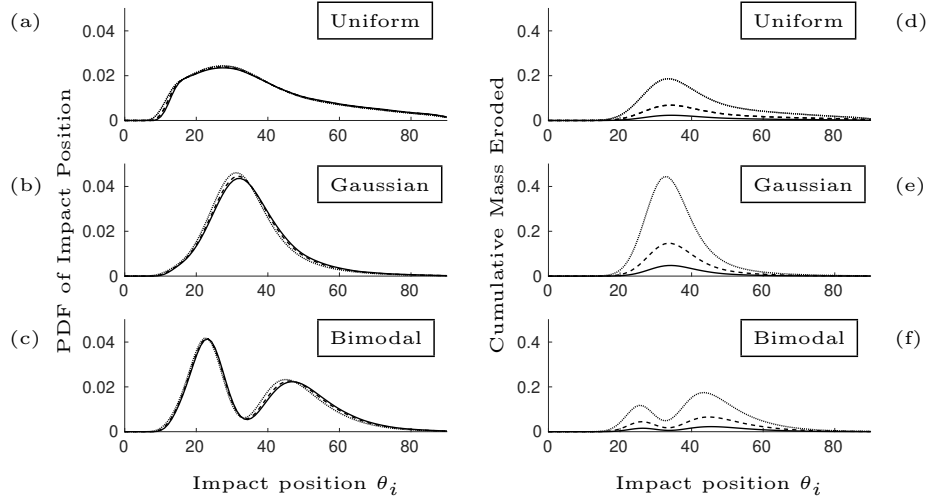


Figure 12: Left panel (a,b,c): probability distribution function (PDF) counting the frequency of impact along the bend by impact position  $\theta_i$ . Right panel (d,e,f): cumulative mass  $m$  eroded as a function of impact position. The solid curves represent 50,000 cycles, dashed curves represent 125,000 cycles, and dotted curves represent 250,000 cycles. Each curve is a statistical representation of the cumulative erosion, in terms of location and mass, by a single particle according to Algorithm 2 with  $M = 20$  particles. In the rows, we distinguish the results with entry positions, over 250,000 cycles, taken from the uniform, Gaussian ( $\nu = 0.4$ ), and bimodal ( $q = 0.5, \nu = 0.2$ ) distributions (Eq. 20) respectively. In all simulations,  $\chi = 10\%$ .

434  $R_0 > R$  than with  $R_0 < R$ . However, though particles entering with  $R_0 < R$   
435 impact with a wider distribution, two additional factors are also present:  
436 (i) the aforementioned larger velocity and (ii) the corresponding impact an-  
437 gle  $\alpha$  (Figure 3(d)) so that  $f(\alpha)$  (Eq. 12) is larger. These two factors in fact  
438 combine multiplicatively to increase the volume eroded in (Eq. 14), in accor-  
439 dance with (Eq. 18). This trade-off in impact frequency and volume eroded  
440 dramatically affects the erosion process depending on the inlet distribution.

441 This trade-off is most easily seen with the bimodal distribution (Fig-  
442 ure 12(c,f)). Two equal peaks in the inlet distribution result in one larger  
443 narrow peak and one smaller wide peak in the impact locations. However,  
444 more mass is eroded from an impact zone with lower overall frequency but  
445 greater impact speed. This feature is not so easily seen in the uniform (Fig-  
446 ure 12(a,d)) and Gaussian (Figure 12(b,e)) distributions that have a single  
447 peak in the probability density of impact positions, though a subtle shift in  
448 skewness is present.

449 The uniform distribution has the most widespread resulting impact angle  
450 distribution (Figures 12(a)), as expected. There is a central peak at  $\theta_i = 28^\circ$ .  
451 This peak does not change as the particle grows and the Stokes number  
452 increases. However, about that peak point, the impact distribution shifts to  
453 lower values, again as expected. Furthermore, there is an asymmetry about  
454 the peak with the frequency of impact higher to the left than right. This is  
455 due to the spread of impact angles of particles entering with  $R_0 < R$ .

456 The Gaussian distribution produces a narrow peak in impact position  
457 (Figures 12(b)). Overall, this distribution shifts to lower values as the particle  
458 grows, with the peak at  $\theta_i = 33^\circ$  shifting to  $31^\circ$ . The cumulative mass eroded

459 by position in the bend (Figures 12(e)) is much greater than the uniform case  
460 (Figures 12(d)) because of the increased frequency of impact, as expected.

461 The most interesting case is the bimodal distribution. Here the two peaks  
462 in inlet particle distribution produce very different impact position distribu-  
463 tions (Figures 12(c)) and cumulative mass erosion (Figures 12(f)). Particles  
464 entering with the inlet bimodal peak at  $R = 8.5 > R_0$  produce a higher  
465 narrower impact position peak compared to those entering with the inlet bi-  
466 modal peak at  $R = 7.5 < R_0$ . Again this is because of the Poiseuille flow  
467 that particles entering at  $R < R_0$  must traverse. Over 50,000 impacts, the  
468 impact position peaks shift, and that shift is more pronounced in the lower  
469 impact position peak:  $\theta_i = 23^\circ \rightarrow 22^\circ$  and  $\theta_i = 46^\circ \rightarrow 44^\circ$ . However, in  
470 terms of erosion, the peak with lower frequency has a greater erosion effect.  
471 Again, this is attributed to the speed of the particle upon impact.

472 Note that the peak of cumulative mass erosion by the uniform (Fig-  
473 ure 12(d)) and bimodal (Figure 12(f)) distributions take similar values, but  
474 only the bimodal impact angle distribution has a shift in the peak. This is  
475 again because of the location of the entry position corresponding to each im-  
476 pact position peak. Particles in the bimodal system impacting at that peak  
477 enter to the left of the channel centre with an associated higher velocity upon  
478 impact.

479 The rate at which particles do not impact the wall decreases approxi-  
480 mately linearly with cycle time (Figure 13), with the largest rate for the  
481 uniform distribution. This is due to the increased likelihood (Figure 7) of a  
482 particle entering from a position nearer the walls whereby impact does not  
483 occur. Recall in Figure 5 that the range of inlet positions with no impact

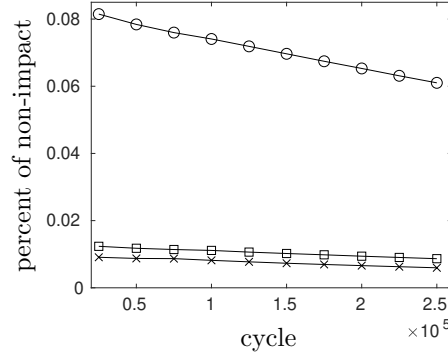


Figure 13: The percentage of particles that do not impact the walls when passing through the bend as a function of cycle time for the three distributions: uniform ( $\circ$ ), Gaussian ( $\times$ ) with  $\nu = 0.4$ , and bimodal ( $\square$ ) with  $q = 0.5$  and  $\nu = 0.2$ . This percentage decreases approximately linearly with the greatest rate observed with the uniform distribution. In all simulations,  $\chi = 10\%$ .

484 occurring decreases as the Stokes number increases.

## 485 6. Conclusions & Discussion

486 In this paper, we have modelled particle impact and erosion at a  $90^\circ$  bend  
 487 in a channel Poiseuille flow. Particles deviate from the flow in the bend and  
 488 impact the channel wall. The motion and impact properties depend on the  
 489 parameters of inlet position and Stokes number. We analyse time, location,  
 490 angle, and velocity of impact based on these parameters. Finnie's model<sup>???</sup>  
 491 is used to calculate material erosion. We developed this model to account  
 492 for the evolving erosion process.

493 We illustrated the erosion characteristics with statistics based on three  
 494 inlet distributions: uniform, Gaussian, and bimodal. These represent well-

495 mixed, concentrated, and tubular-pinch distributions respectively. Adhesion  
496 of any amount leads to exponential growth in erosion along the bend. The  
497 additional exponential erosion is similar for a uniform and bimodal particle  
498 distribution, but greater for a Gaussian distribution. Furthermore, we show  
499 how the growing particle erodes more material at shifting location distribu-  
500 tions. As particles grow in size, the impact site probability density functions  
501 shift to lower values due to the change in Stokes number altering the particle  
502 trajectories and speeds from the inlet positions. This means that the section  
503 of wall most impacted changes with time. However, the rate of erosion does  
504 not always follow this pattern. For the bimodal distribution, the influence  
505 of the flow on a particle entering the bend about one of the peaks spreads  
506 out the corresponding impact site compared to the other peak. However,  
507 that same flow increases the particle impact velocity so that more material  
508 is eroded throughout the overall less-frequently (more spread out) impacted  
509 region.

510 The methodology outline here may readily be scaled up to any number of  
511 particles, within a dilute limit, incorporating delays to represent the intro-  
512 duction of new particles by corrosive effects. The model we have presented  
513 should provide a basis to understand the deleterious effects of erosion in a  
514 range of industrial piping systems. We highlight the exponentially detrimen-  
515 tal effects of erosion in a closed channel, and appeal to the wider community  
516 for experimental or CFD simulations to validate our model. We note that  
517 the exponential effects are only observed over a long timescale. As a result,  
518 our simple model is a guide for tuning computationally expensive CFD sim-  
519 ulations. In addition, our mathematical model is able to quickly provide

520 long-term predictions that which would be prohibitively time consuming to  
521 obtain experimentally.

522 Our model may be adjusted or improved in a number of ways for dif-  
523 ferent operating and physical conditions. As mentioned, in the case of non-  
524 laminar and higher-Reynolds-number flows, a boundary layer correction?  
525 in the curved section may be imposed and a quadratic velocity-dependent  
526 drag? may be applied to the particle transport. For particular materials  
527 or extreme operating conditions (impact speed and temperature), Finnie's  
528 model may be updated to incorporate a plastic deformation component? ,  
529 allowing for erosion at high impact angles? . The volume of eroded material  
530 adhering to the impacting particle may be adjusted by a factor, either deter-  
531 ministically or stochastically, to capture the practical nature of erosion? ? ? .

## 532 **Acknowledgements**

533 This publication is based on initial work supported by Award No. KUK-  
534 C1-013-04, made by King Abdullah University of Science and Technology  
535 (KAUST). IMG gratefully acknowledges support from the Royal Society  
536 through a University Research Fellowship.